Carbohydrate Polymer Technologies and Applications 2 (2021) 100083

Contents lists available at ScienceDirect

Carbohydrate Polymer Technologies and Applications

journal homepage: www.elsevier.com/locate/carpta

Design of super-paramagnetic bilayer films based on chitosan and sodium alginate

Gianina A. Kloster[a], Oscar Moscoso Londoño[b,c], Kleber R. Pirota[b], Mirna A. Mosiewicki[a], Norma E. Marcovich[a,d,*]

[a] Instituto de Investigaciones en Ciencia y Tecnología de Materiales (INTEMA), Facultad de Ingeniería, Universidad Nacional de Mar del Plata (UNMdP) – Consejo Nacional de Investigaciones Científicas y Técnicas (CONICET), Mar del Plata, Argentina
[b] Instituto de Física Gleb Wataghin (IFGW), Universidade Estadual de Campinas – UNICAMP, Campinas, São Paulo, Brazil
[c] Universidad Autónoma de Manizales, Facultad de Ingeniería, Antigua Estación del Ferrocarril, Manizales, Colombia
[d] Departamento de Ingeniería Química y en Alimentos, Facultad de Ingeniería - UNMdP, Mar del Plata, Argentina

ARTICLE INFO

Keywords:
Nanocomposite bilayer films
Chitosan
Sodium alginate
Iron oxide nanoparticles
Super-paramagnetic behavior

ABSTRACT

Bilayer films that combine chitosan and alginate, two natural polysaccharides, and magnetic iron oxide nanoparticles (MNPs) were obtained. Physical and microscopic observations revealed that chitosan and alginate interact strongly through their surfaces, which is attributed to the formation of a polyelectrolyte complex at the interface. The diameter of the individual MNPs was about 10 nm, although in the films they appear arranged in clusters with sizes ranging from 23 nm to several times larger that are formed by collapsed individual particles. All bilayers containing MNP behave as super-paramagnetic materials, exhibiting magnetic synergic effects in comparison to single carbohydrate films. Thus, obtained films could find novel and interesting applications as pH responsiveness systems, pad dressings including hyperthermia, adsorption of positive and negative charged pollutants, etc.

1. Introduction

It is currently known that nanomaterials show distinctly different physicochemical properties from their bulk counterparts, resulting in unique thermal, optical, electric and magnetic properties of materials, which open new areas of their possible applications (Piosik, Klimczak, Ziegler-borowska, & Chełminiak-dudkiewicz, 2020). Thus, it is not surprising that magnetic nanoparticles have attracted considerable attention among nanomaterials in recent years, due to their application potential in information and energy storage, sensors, medicine, etc. (Piosik et al., 2020). In this line, magnetic iron oxide nanoparticles (MNP) have been intensively studied for several medical and biotechnological applications because they show attractive characteristics as super-paramagnetic behavior (high magnetization saturation and magnetic susceptibility), high ratio surface/volume, chemical stability, low toxicity, biodegradability, biocompatibility and ease of synthesis (Fang, Bhattarai, Sun, & Zhang, 2009; Karimi, Karimi, & Shokrollahi, 2013; Xu et al., 2012). Among the sixteen types of iron oxides reported in the literature, those formed from Fe^{2+} and Fe^{3+} ions are magnetic in nature (Siddiqui & Chaudhry, 2017), but the most actively investigated forms are the MNPs of magnetite (Fe_3O_4) or maghemite (γ-Fe_2O_3) with diameters between of 5–20 nm (Karimi et al., 2013). Magnetite contains divalent iron, Fe^{2+}, and trivalent iron, Fe^{3+}, arranged in a face-centred cubic (fcc) crystal structure. It is oxidized by air even at room temperature and thus transforms into maghemite, which is isostructural with magnetite. Maghemite (containing only trivalent iron in its structure) can further transform into hematite (α-Fe_2O_3) at temperatures above 300 °C. Thermal transformation of various iron oxides leads ultimately to hematite, which is thermodynamically most stable and most abundant in natural systems (Cornell & Schwertmann, 2003; Siddiqui & Chaudhry, 2017).

One of the interesting uses of iron oxide particles is the removal of contaminants such as heavy metals, arsenic and organic pollutants (Iram, Guo, Guan, Ishfaq, & Liu, 2010; Nassar, 2010; Siddiqui & Chaudhry, 2017), although several authors recommend coating these nanoparticles to prevent oxidation and aggregation (Li et al., 2017). As an alternative, nanoparticles can also be loaded in macroscopically solid materials, which can fulfill the previous functions and, simultaneously avoid secondary pollution to the environment caused by their very minute dimensions (Li et al., 2017).

The interest in using biobased materials as holding matrices for the synthesis of nanocomposite materials has also increased in the last years

* Corresponding author at: Institute of Materials Science and Technology (INTEMA) - CONICET / Engineering Faculty - National University of Mar del Plata (UNMdP). Juan B. Justo 4302, 7600 Mar del Plata, Argentina.
E-mail address: marcovic@fi.mdp.edu.ar (N.E. Marcovich).

https://doi.org/10.1016/j.carpta.2021.100083
Received 15 January 2021; Received in revised form 19 April 2021; Accepted 28 April 2021

as a response towards solving the advancement of environmental issues, which adds to the large availability of these raw materials and their inherent biodegradability (George, Sanjay, Sriusk, Parameswaranpillai, & Siengchin, 2020; Meiorin, Muraca, Pirota, Aranguren, & Mosiewicki, 2014). Chitosan and sodium alginate are natural polymers, which are nontoxic, biodegradable, biocompatible and pH sensitive (Lacerda, Parize, Fávere, Laranjeira, & Stulzer, 2014). Chitosan is a biopolymer derived from the partial deacetylation of chitin, the major component in the shell of arthropods and cell wall of fungi. Chitosan is mainly a linear polymer of β-(1-4)-linked d-glucosamine and N-acetyl-d-glucosamine (Matet, Heuzey, Pollet, Ajji, & Avérous, 2013) and a cationic polyelectrolyte because of the presence of amino groups. On the other hand, sodium alginate is a polysaccharide extracted from marine brown algae, made up of linear chains of α-L-glucuronic acid (G) and β-D-mannuronic acid (M) (Norajit, Kim, & Ryu, 2010; Rafiee et al., 2014). This biopolymer is water-soluble and because it contains carboxylate groups, it is also an anionic polyelectrolyte. Both biopolymers show good properties as film formers and very interesting chelating properties (Wang, Sun, & Yang, 2014) due they contain functional groups as amino and hydroxyl (chitosan), and carboxylate and hydroxyl (alginate). Furthermore, when they are mixed, a polyionic complex is formed through the ionic gelation via interactions between carboxyl groups of alginate and protonated amine groups of chitosan (Han, Dong, Song, Yin, & Li, 2014; Motwani et al., 2008). This complexation can also occur on the surface of a film, leading to bilayer films that can better exhibit the unique properties of the substrates (Zhu, Wu, & Sun, 2019).

Thus, the combination of chitosan and sodium alginate to form a membrane has been studied in several works, leading to materials suitable for different applications such as drugs controlled release (Tian, Xie, & Xia, 2013), anti-adhesion barrier to prevent peritoneal adhesions (Chang, Lee, Wu, Yang, & Chien, 2012), wound dressing applications (Dong et al., 2010; Han et al., 2014), pervaporation, dehydration (Kanti, Srigowri, Madhuri, Smitha, & Sridhar, 2004) and adsorption of different pollutants (Agostini de Moraes, Cocenza, da Cruz Vasconcellos, Fraceto, & Beppu, 2013; Carneiro et al., 2015; Cocenza, De Moraes, Beppu, & Fraceto, 2012). However, the incorporation of a magnetic phase in this kind of membranes has not been enough analyzed although it could provide the material with new and interesting properties, such as regulating the release of biomolecules loaded in the different layers by varying both, the intensity and the frequency of the applied magnetic field (Brazel, 2009; Edelman & Langer, 1993) or to control the adsorption/desorption of species by changing the temperature of the bilayer composite by magnetic heating (Eivazzadeh-Keihan, Radinekiyan, Asgharnasl, Maleki, & Bahreinizad, 2020). Even so, and as far as we know, the only work that explores this possibility was published by Criado et al. (Criado et al., 2016), who prepared multilayers of alginate-chitosan with iron oxide nanoparticles through spray assisted layer-by-layer assembly, suggesting that these complex films have potential to be used as dermal pads for local magnetic hyperthermia.

We have already prepared and characterized films based on an individual biopolymer, i.e. chitosan or sodium alginate, and iron oxide nanoparticles using two different obtaining methods (Kloster, Marcovich, & Mosiewicki, 2015; Kloster et al., 2018, 2020; Kloster, Muraca, et al., 2015; Kloster, Muraca, Mosiewicki, & Marcovich, 2017). In this work, we prepared composite bilayer films using chitosan and sodium alginate as the individual continuous phases by adding different amounts of MNP to each layer, using both polymeric matrices into a composite material. Morphological and magnetic characterization was performed to analyze the effect of the MNP content and their distribution in each layer on the final properties of the composite films. Even though possible applications for the bilayers are not analyzed in this work, this new material could be useful for different technological fields, such as applications that involve pH responsiveness (i.e. pH induced bending by alginate layer swelling at alkaline pH or chitosan swelling at acidic pH), wound dressings including magnetic heating, adsorption of pollutants with both, positive and negative charges, among others.

2. Experimental

2.1. Materials

Chitosan (CH, degree of deacetylation 98%, Mv = 1.61×10^5 g/mol) in powder form supplied by Parafarm (Argentina) and sodium alginate (SA, moisture content $\leq$ 14.1%; viscosity (1% in water) = 19 cps) in powder form supplied by Sigma Aldrich (Argentina) were used as received. Glycerol purchased from DEM (Mar del Plata, Argentina) was used as plasticizer. Ferric chloride ($FeCl_3.6H_2O$), ferrous sulphate ($FeSO_4.7H_2O$) and ammonium hydroxide (25% NH_3) were obtained from Aldrich (Argentina).

2.2. Methods

2.2.1. Synthesis of magnetic iron oxide nanoparticles (MNP)

The iron oxide was made by a co-precipitation method adopted in previous works (Kloster et al., 2018). Briefly, $FeCl_3.6H_2O$ and $FeSO_4.7H_20$ salts were dissolved in distilled water in order to obtain a Fe^{+2}:Fe^{+3}=1:2 molar ratio. Once the solution was perfectly homogeneous, ammonium hydroxide was added drop by drop to avoid or minimize the iron oxide aggregation. The suspension was stirred for 15 minutes, allowing the complete precipitation of MNP. After this time and with the help of a magnet placed out of the flask, the precipitated particles were washed several times with distilled water until reaching neutral pH. Finally, the obtained particles were placed into a Petri plate and lyophilized to eliminate the remaining water. The complete characterization of the obtained MNP was previously reported (Kloster et al., 2018) although it should be pointed out that an average particle diameter of 9.5 ± 2 nm with a narrow size distribution was calculated by the statistical analysis of the particle diameter measured from transmission electron microscopy (TEM) images.

2.2.2. Preparation of composite bilayer films

Bilayer films were prepared by traditional casting of the film forming solutions into Petri dishes (diameter = 14 cm) followed by solvent (water) evaporation, adding the chitosan solution once the alginate layer was totally dried. Each layer was successively dried in a convection oven at 35°C for 24 h. Alginate film forming solution (pH 7.4) was obtained by dissolving 1 g alginate in 50 mL distilled water while chitosan solution (pH 4.7) was prepared by dissolution of 1 g chitosan in 50 mL aqueous acetic acid (1% v/v) by magnetic stirring. In both cases, glycerol, the plasticizer selected for both systems, was added in a 30 wt% respect to the carbohydrate mass. To prepare magnetic films, 3, 5, 7 and 10 wt% of MNPs (calculated respect to the carbohydrate weight of each filmogenic solution) were incorporated into the corresponding film forming solution and suspended by ultrasonication for 2 h. Composite bilayer films were prepared as described previously but replacing the film forming solution by the corresponding MNPs suspension. Finally, the bilayer films were kept in a closed container containing dried silica gel at room temperature (23 ± 2°C) until testing. Obtained films were labeled according to the MNP weight content (% MNP in the alginate layer-% MNP in the chitosan layer) as 0-0, 3-3, 5-5, 7-7, 10-10.

2.2.3. Characterization of bilayers

Film thickness: The thickness of the bilayer films was measured with a manual micrometer with an accuracy of ± 0.01 mm at least at five random locations for each sample. The reported values are the average of those individual measurements.

Fourier-transform infrared spectroscopy (FTIR): FTIR spectra of the films were recorded by the attenuated total reflection method (ATR) using a Thermo Scientific Nicolet 6700 Fourier transform infrared spectrometer (Madison, WI, USA). The spectra were recorded over a range of 500–4000 cm^{-1} with a resolution of 2 cm^{-1} and averaged over 32 scans, on both sides of the bilayers.

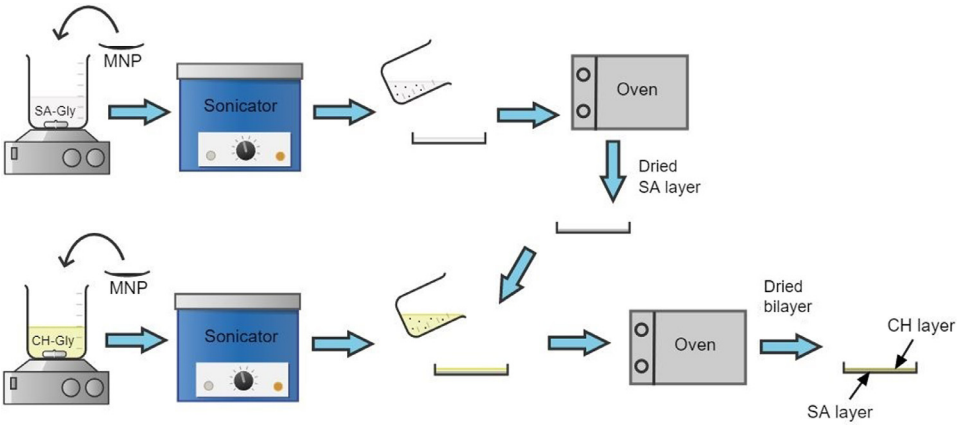

Scheme 1. Schematic representation of the adopted methodology for the preparation of composite bilayer films.

Raman spectroscopy: Raman spectra were obtained using a Renishaw InVia reflex system (United Kingdom) equipped with charge-coupled device (CCD) detector of 1040 × 256 pixels. A 785 nm diode laser (300 mW) was used as excitation source, in combination with a grating of 1200 lines/mm. A 50X (0.5 NA) long working distance (8 mm) Leica metallurgical objective was used in the excitation and collection paths. Spectra were typically acquired in 5 s with at least 4 accumulations.

X-ray diffraction (XRD): The structure of the composites was evaluated from the X-ray diffraction patterns of the different films, which were obtained using CuKα radiation (λ=1.5418 A) in a PANalytical X'Pert Pro diffractometer (Egham, Surrey, United Kingdom) operated at 40 kV, 300 mA and 0.6 °C/min. The average crystallite grain size was calculated applying the Scherrer equation and assuming spherical structures (Chen, Yang, Ma, & Wu, 2011):

$$\tau = \frac{0.9\lambda}{\beta \cos\theta} \quad (1)$$

where τ is the mean size of the ordered (crystalline) domains, λ is the wavelength of the X-ray (0.1546 nm), θ is the diffraction angle in degrees, and β in radians is the measured full width at half maximum intensity. The diffraction peak at 2θ = 35.5°, which corresponds to the lattice plane (3 1 1), was used for calculation.

Scanning Electron Microscopy (SEM): The cross section of the bilayers (obtained by cryo-fracture after immersing samples in liquid air), were analyzed using a scanning electron microscope (JEOL, model JSM-6460 LV, Tokyo, Japan). For this purpose, the pieces of the films were mounted on bronze stubs using a double-side tape and then coated with gold, to be later observed under the microscope.

Field Emission Scanning Electron Microscopy (FESEM): The cross sections of the bilayer films (obtained by cryo-fracture after immersing samples in liquid air) were analyzed with a Carl Zeiss Supra 40 Gemini, Field Emission Scanning Electron Microscope (FESEM, Germany). Samples were mounted on an aluminum disc using sticky conducting tape to fix them.

Small-angle X-ray Scattering (SAXS): SAXS experiments were performed on SAXS1 beamline at the Brazilian Synchrotron Light Laboratory (LNLS), Centro Nacional de Pesquisa em Energia e Materiais (CNPEM), Campinas, Brazil. The measurements were carried out at room temperature. The scattering intensity was recorded as function of momentum transfer vector q (q = 4π sinθ/λ), in a range from 0.1 to 5.0 nm^{-1}, being θ the scattering angle and λ the wavelength = 1.822 Å.

Magnetic characterization: The magnetic properties of the composites were obtained using a SQUID magnetometer (Quantum Design, MPMS XL, USA). Both isothermal magnetization curves, as well as the magnetizations vs. temperature function measurements, were performed in order to characterize the magnetic properties of the nanocomposite films. The magnetization (M) vs. applied field (H) curves were recorded at 5 and 300 K in a magnetic field range of ± 20 kOe. The dependence of magnetization on temperature was obtained under the zero-field-cooling and field-cooling (ZFC/FC) protocols with a static magnetic field of 50 Oe in a temperature range of 5 to 300K.

3. Results and discussion

3.1. Physical and chemical characterization

The obtained bilayer films exhibit some irregularities in their surfaces (images not shown), which are thought to have formed after casting the chitosan solution on the dried alginate layer, as summarized in Scheme 1. The average thickness of all dried samples was among 120 to 160 μm, without observing statistically significant differences as a function of the MNPs content. Concerning resistance to solvents, the bilayers lost part of their weight (about 12% and 9% for the 0-0 and 10-10 bilayer films, respectively) after immersing square samples of 1 cm x 1 cm area in 5 mL ethanol or acetone (as examples of polar organic solvents) for 24 h, which was attributed mainly to the lost of glycerol, since the specimens retained their structural integrity. On the other hand we were able to confirm the insolubility of the samples in chloroform (selected as example of the non polar solvents). Regarding their behavior in water, most of the alginate layer dissolves during testing at the same time that the whole bilayer swells, which complicates the measurement, deserving additional tests and further analysis that will be part of a future publication.

ATR spectra were obtained measuring on both sides (chitosan and alginate layers). Fig. 1a shows the spectra obtained for bilayer 0-0 in comparison with the spectra of the single plasticized polymers molded as monolayers. It can be noticed that the spectra of the bilayers are very similar to the corresponding to those of the single carbohydrates. For chitosan side, a broad band centered on 3300 cm^{-1} related to -OH hydrogen bonded with contribution of the -NH_2 group- stretching vibration (Pawlak & Mucha, 2003) can be noticed. The bands at 2920 and 2876 cm^{-1} are due to the CH_2 and CH tertiary groups. The band at 1650 cm^{-1} corresponds to the C=O stretching vibration of the amide band (Pereda, Aranguren & Marcovich, 2007). The band at 1560 cm^{-1} is indicative of NH-bending vibration in amide groups. The band centered at 1400 cm^{-1} is assigned to the combined in-plane bending vibrations of -CH_2 in CH_2OH groups and -CH_3 in $NHCOCH_3$ groups, while the shoulder observed at 1320 cm^{-1} is attributed to in-plane bending vibrations (C-H) in pyranose ring (Kaya et al., 2014; Zvezdova, 2010). The band at 1150 cm^{-1} is related to the -C-O-C- vibration of the glycosidic linkage (Pawlak & Mucha, 2003). The small peak at 900 cm^{-1} corresponds to the β linkage of the glucoside rings (Pereda, Aranguren, & Marcovich, 2007). On the other hand, the FTIR spectra of sodium alginate as well as that of the alginate side of the bilayer film display a broad band between 3600 and 3000 cm^{-1} corresponding to the contribution of the -OH group vibration that comes from the polymer and plasticizer (glycerol). The peaks at 2930 and 2875 cm^{-1} are assigned to the asymmetric and sym-

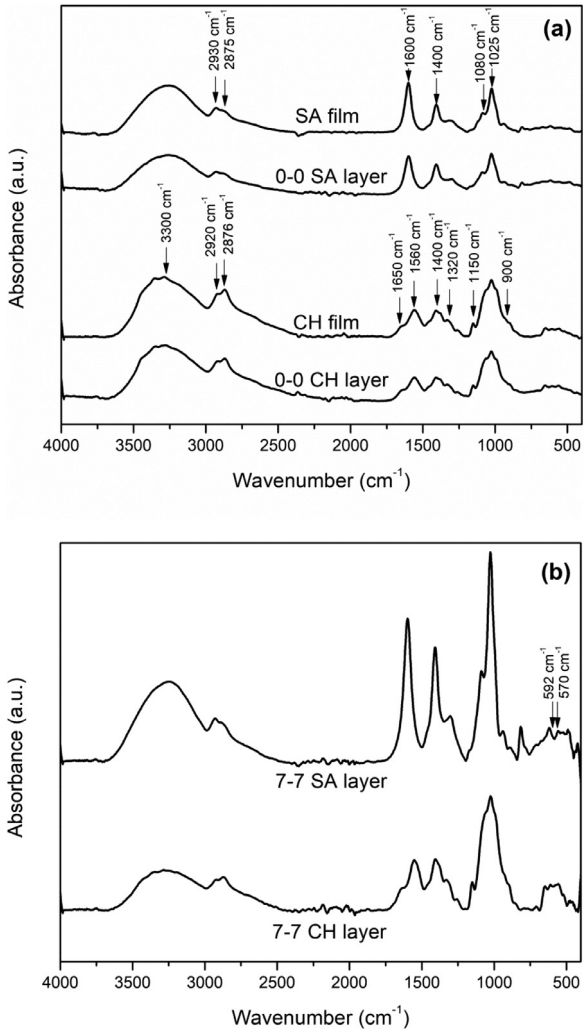

Fig. 1. (a) FTIR spectra of the single plasticized films (SA, CH) and bilayer 0-0 tested on both sides. (b) FTIR spectra of the composite bilayer 7-7.

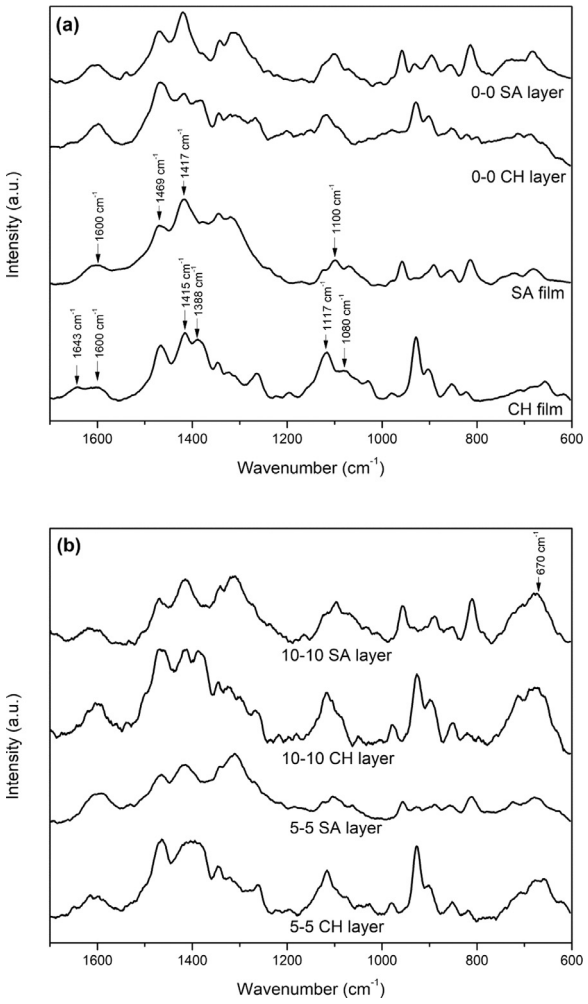

Fig. 2. (a) Raman spectra of CH and SA plasticized films and CH and SA layers corresponding to the 0-0 bilayer film. (b) Raman spectra of 5-5 and 10-10 bilayer films.

metric stretching vibrations of the aliphatic C-H group (Daemi, Barikani, & Barmar, 2013). The peaks at 1600 y 1400 cm^{-1} correspond to the antisymmetric and symmetric stretching vibrations of the carboxylate anion (COO^-) of alginate and the bands located at 1025 and 1080 cm^{-1} are related to its glucosidal linkages (C-O-C groups asymmetric stretching) (Agostini de Moraes et al., 2013; Lakouraj, Mojerlou, & Zare, 2014).

Several works report the emergence of new bands after the formation of the chitosan-alginate membrane. These new bands appear at 1639 cm^{-1} due to symmetric -NH_3C deformation and at 2500 and 1900 cm^{-1} because to the presence of -NH_3C group (Elmotasem, 2008; Kanti et al., 2004; Smitha, Sridhar, & Khan, 2005). Those works are based on the mix of the two polymers, where the interaction between both carbohydrates is in bulk. In this work, these characteristic bands associated with the formation of chitosan-alginate complex are not observed because polymers interact only at the interface, within a small thickness compared with the total bilayer. Besides, this interfacial region is far from the infrared radiation range region, i.e., the radiation is completely attenuated at ~ 1-2 μm from the surface of the glass, while the interface is located approximately at 60 μm from the beam incidence surface. In addition, the layers seem to be well differentiated, which means that the interaction of the polymers is occurring only in the interfacial region (a small region with a few micrometers of thickness). Therefore, the limitations of this technique do not allow us to confirm neither the polyion complexation of both carbohydrates due to ionic cross-linking at the interphase nor any other kind of interaction between alginate and chitosan.

On the other hand, the presence of iron oxide MNPs is clearly observed in the FTIR spectra of 7-7 composite film (Fig. 1b), where a set of bands between 650 and 560 cm^{-1}, characteristic of Fe–O–Fe bond, are displayed (Abbaszad Rafi & Mahkam, 2015). Specifically, the band centered at 592 cm^{-1} corresponds to Fe-O stretching vibration in tetrahedral sites (Xuan Nui, Tan Phuoc, Tuyet Nhung, Thi Thuy Nga, & hi Van Thi, 2016) while the band located at 570 cm^{-1} is typical for magnetite (Fe_3O_4) and maghemite (γ-Fe_2O_3), which are isostructural (Lassalle, Zysler, & Ferreira, 2011). Clearly, the signals of the single carbohydrates (chitosan or alginate) are again visible depending on the assessed side.

It is well-known that infrared and Raman spectroscopic techniques are complementary for the structural analysis of molecules. Since they differ in selection rules, bands due to vibrations changing molecular polarizability are easily detectable in Raman spectra whereas motions, which change of dipole moment, can be better recognized by IR spectroscopy (Wiercigroch et al., 2017). Thus, the Raman spectra of selected samples were also obtained and analyzed. Fig. 2 a displays the Raman spectra of plasticized chitosan and alginate individual layers added to the corresponding to chitosan and alginate sides of the bilayer film (without iron oxide MNPs), taken in the thickness of each layer. In the spectrum of chitosan, the absorption band of the carbonyl (C=O) stretching of amide I appears at 1643 cm^{-1} and the bending vibrations of the N–H (N-acetylated residues, amide II band) at 1600 cm^{-1} (Sanna et al., 2012; Zając, Hanuza, Wandas, & Dymińska, 2015).

The band appearing at 1415 cm^{-1} is associated with the vibrations of polysaccharide backbones (in-plane bending vibrations of CH_3 and CH groups) (Reinas, Hoscheid, Outuki, Lane, & Cardoso, 2014; Zając et al., 2015). The band at 1388 cm^{-1} belongs to the N–H stretching of the amide. The peaks observed at 1080 and 1117 cm^{-1} are characteristic of C–O stretch of –CH–OH in cyclic alcohols and of $-CH_2-OH$ in primary alcohols, respectively (Sanna et al., 2012). Regarding the alginate film, Raman spectroscopy shows a band around 1100 cm^{-1} due to C–O–C stretching attributed to its saccharide structure. In addition, the bands at 1600 and 1417 cm^{-1} were assigned to asymmetric and symmetric stretching peaks of carboxylate salt groups (Sanna et al., 2012). The band at 1469 cm^{-1} could be attributed to the appearance of the carboxyl ion stretch (typical for alginic acid salts) as a consequence of the partial protonation of Na-alginate (Gonzalez, Mijangos, & Hernandez, 2019). Concerning Raman spectra of the bilayer film, those peaks that correspond to each individual polymer can be detected in both layers, although they present different intensities mainly in the region of 1500-1300 cm^{-1}, which means that some degree of mixing among carbohydrates was achieved still quite far from the interface.

Raman spectra of chitosan and alginate layers of the composite films containing 5 (5-5 sample) and 10 wt% magnetic nanoparticles (10-10 sample) are shown in Fig. 2b. Both sides of the bilayer film exhibit peaks around 670 cm^{-1} that can be attributed to the iron oxide particles (Shebanova & Lazor, 2003; Slavov et al., 2010). In fact, the peak at 670 cm^{-1} is typical of the spinel ferrite, due to the A1g mode corresponding to the O atoms symmetrically stretching along with the Fe-O bond at the tetrahedral locations (Bartůněk et al., 2018; Guo, Hu, Qian, Ning, & Xu, 2011; Shebanova & Lazor, 2003). While both individual polymers present Raman signals between 650 and 700 cm^{-1}, as can be noticed from Fig. 2a, the intensity of this zone increases as the amount of MNPs in the sample increases since becomes overlapped with signal coming from the magnetic filler (Wang et al., 2003), although the level of interactions among chitosan/alginate and iron oxide nanoparticles cannot be determined by IR or Raman spectroscopies. In fact, it is explained through complex mechanisms of electrostatic forces and interactions occurring between polar groups, as was reported in previous papers (Kloster, Marcovich, et al., 2015; Kloster et al., 2018, 2020) and related works (Cesano, Fenoglio, Carlos, & Nisticò, 2015; Xu, Shen, Xu, Xie, & Li, 2006).

X-ray diffraction patterns of the individual plasticized carbohydrate films (a) and selected bilayers (b) (0-0, 5-5 and 10-10) are shown in Fig. 3. The characteristic peaks of magnetite/maghemite appear in all composite bilayers, with intensities depending on the MNP concentration. These characteristic peaks can be seen at $2\theta = 30.1^{\circ}$, 35.5°, 43.3°, 53.4°, 57.2° and 62.8° and can be indexed to (2 2 0), (3 1 1), (4 0 0), (4 2 2), (5 1 1) and (4 4 0) planes, respectively, which correspond to crystals with cubic crystalline structure (Bhatt, Krishna Bhat, & Santosh, 2010; Zhang et al., 2010). From the broadness of the diffraction peaks, crystallite size of the MNP was determined using Scherrer's equation (Patterson, 1939), obtaining a diameter of 9.5 nm for synthesized neat MNP (Kloster et al., 2018) and 10.5 nm for particles included in the 10-10 bilayer. Despite that "crystallite size" is not necessarily synonymous of "particle size", this method can provide an estimation of the diameter of the magnetic particles (Kloster et al., 2018) that, in the present case, largely coincides with the dimensions obtained for the neat MNP by TEM microscopy, as was reported in previous works (Kloster et al., 2018, 2020).

In Fig. 3 a the patterns obtained for each single polymer are shown. Chitosan film shows crystalline peaks at 9°, 12° y 18°, and an amorphous halo centered at 22° (Kloster et al., 2018). On the other hand, for the alginate film, we can observe two peaks related to amorphous regions centered at 13.5° y 21.3° (Kloster et al., 2020). However, in the 0-0 bilayer shown in Fig. 3 b it can be seen that chitosan crystalline peaks appear with reduced intensity while its amorphous halo overlaps with the corresponding to alginate (around 22°). Unlike the FTIR technique, X-ray diffraction measures the whole (bulk) composite, analyzing the

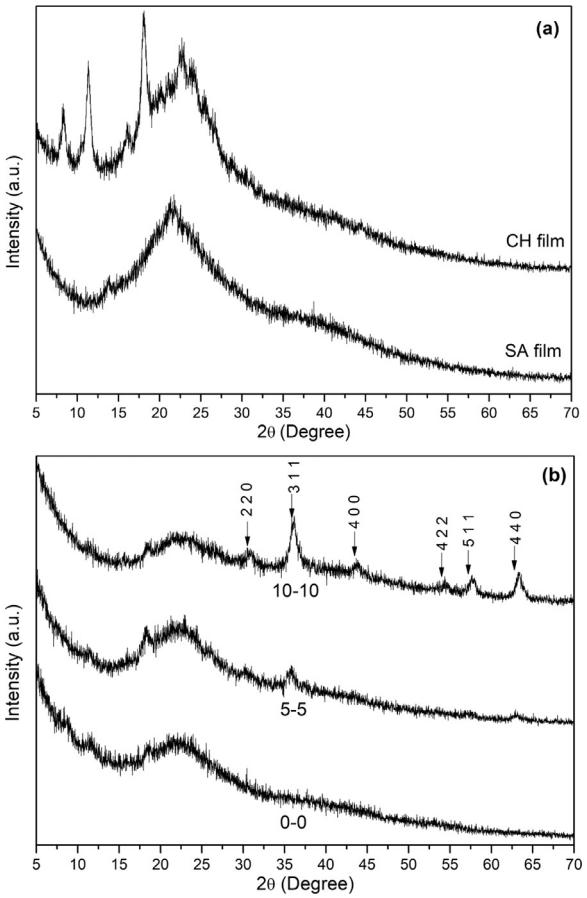

Fig. 3. XRD patterns of (a) CH and SA plasticized films and (b) bilayers 0-0, 5-5 and 10-10.

two layers simultaneously, so that crystalline chitosan peaks no longer look as sharp as when analyzing the chitosan film alone. In other words, the spectrum of the material could be constructed from the sum of the individual spectra of alginate, chitosan and their interface. In the same way, overlapping with the $Fe_3O_4/\gamma Fe_2O_3$ peaks leads to the diffraction pattern of the polymeric matrix appearing with a lower intensity as the MNP content increases.

The morphology of the films was analyzed using SEM microscopy. Fig. 4 shows the cross-sections of the bilayers (obtained in cryo-fracture after immersing the samples in liquid air). The selected images were obtained with relatively low magnification, allowing observing the interfacial region between both polymers. Both bio-polymers show fragile fracture patterns but different microstructure: while chitosan appears to be rougher, alginate is smoother. On the other hand, bilayers containing MNPs present also some cumulus that could correspond to microscopic aggregates of nanoparticles (white dots). Moreover, it is observed that the alginate-chitosan interface is well delimited but does not exhibit defects, voids or layer delamination, implying that the biopolymers interact strongly once the cohesive membrane is obtained (Agostini de Moraes et al., 2013). However, a transition region between the layers is not observed, which would indicate that the strong interaction between both polymers took place only on the surface and thus, no interpenetration occurs.

To further analyze the films microstructure, FESEM images of the composites were also obtained. Fig. 5 shows the cross section of the bilayer 5-5 with magnifications on each side. In both layers, it can be observed different sizes of structures (white shapes) related to the presence of iron oxides, from small agglomerates to relatively large clusters formed by collapsed individual particles.

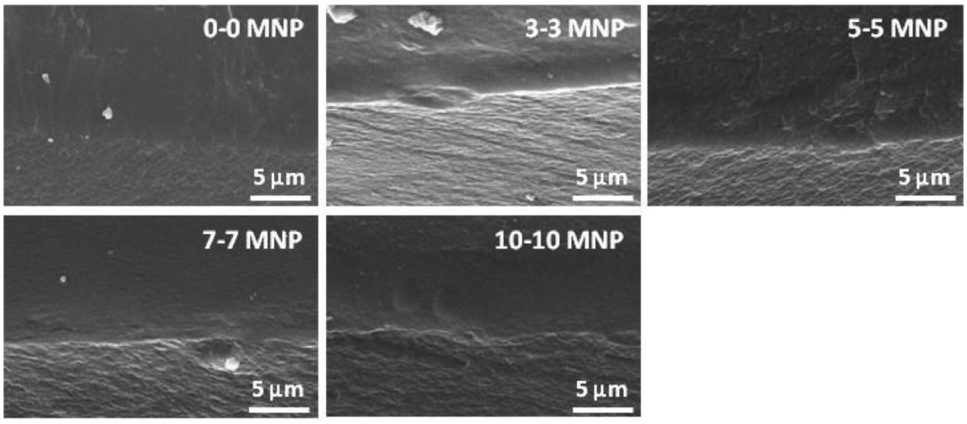

Fig. 4. SEM images of the bilayers in the interfacial zone (layer above: alginate, layer below: chitosan).

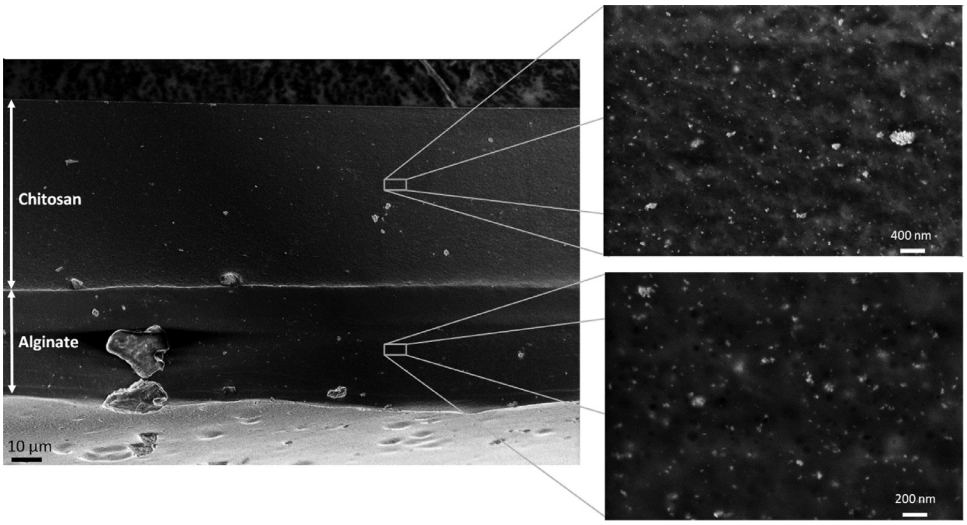

Fig. 5. FESEM images of the bilayer 5-5 and magnifications on each side of the film (above: chitosan, below: alginate)

Therefore, in view of the previous results, SAXS analysis was used to complement the understanding of cluster formation and structural organization of the MNPs into the bilayers. SAXS analysis provides more representative information on particles and aggregates sizes and their distributions (in the scale of nanometers) than imaging techniques (TEM or SEM). Besides, it has a good reproducibility of the results as the averaging depends on a physical effect (Szczerba, Costo, Veintemillas-Verdaguer, Del Puerto Morales, & Thünemann, 2017). However, according to the selected q-range for SAXS tests, the particles or agglomerates that can be identified by this technique have relatively small dimensions, as detailed below.

Fig. 6 shows the log-log representation of scattering intensity (I) versus momentum transfer (q) for the composite bilayers. In all curves we can observe three characteristic regions. In the first region (Guinier region) at low q values ($q < 0.2$ nm^{-1}), the spectra of the bilayers show similar power law behaviors that deviate from the Guinier behavior for non-aggregated entities. However, the Guinier law still can be used if aggregation exists to estimate the radius of gyration (Rg) of particle clusters. Thus, assuming spherical shape, the diameter of the agglomerates was calculated through D = 2 $(5/3)^{0.5}$ Rg. However, according to the q-range used in these tests, only particles/agglomerates with sizes ranging between π/qmax = 1 nm to π/qmin = 30 nm can be identified by this technique. In other words, agglomerates larger than 30 nm are not seen by SAXS technique. As shown in Table 1, diameters of agglomerates around 23 nm were obtained for all composite bilayers, which means that the size of the small agglomerates is independent of the MNP content, a behavior observed in previous works for chitosan and alginate monolayers (Kloster et al., 2018, 2020). In the intermediate zone (0.2 nm^{-1} < q < 0.95 nm^{-1}), the absence of oscillations denotes the existence of particle size distribution of moderate width (Moscoso Londoño et al., 2018). In the Porod zone (high q-region), the scattering intensity behavior can be described with a power law I(q) ~ $q^{-\beta}$, being β the Porod exponent. However, in the present case, the complex nature of

Table 1
Values obtained from fitting SAXS curves obtained from the composite bilayer films.

Bilayer		3-3	5-5	7-7	10-10
Guinier zone	**Rg (nm)**	8.9	9.0	8.0	8.9
	D (nm)	23.0	23.2	23.3	22.9
Porod zone	***β***	-3.8	-3.6	-3.1	-3.3
Beaucage fitting	***G***	2.80E8	4.19E8	9.76E8	3.48E9
	B	1.39E6	3.26E6	3.58E6	6.26E6
	Gs	9.82E7	2.50E8	2.69E8	4.35E8
	Bs	1.62E6	4.19E6	4.86E6	7.84E6
	Rg (nm)	20.81	21.13	20.73	19.38
	Rs (nm)	4.80	4.80	4.80	4.80
	Df	3.04	3.15	3.17	3.16
	P	4.00	4.05	3.99	3.98
	ξ (nm)	53.73	54.56	53.52	50.04

Rg: Gyration radius in the Guinier region; D: cluster diameter in the Guinier region; β: power law of scattering from the Porod zone.
SAXS parameters obtained using Beaucage model (Eq. (2)) with software SASfit. *G:* Guinier pre-factor of larger structures, *B:* Porod pre-factor of larger structures, *Gs:* Guinier pre-factor of smaller structures, *Bs:* Porod pre-factor of the smaller structures, *Rg:* radius of gyration of aggregates, *Df:* fractal dimension, *Rs:* radius of individual particles, *P:* exponent of the power law assigned to the smaller structures, ξ: radius of the agglomerate.

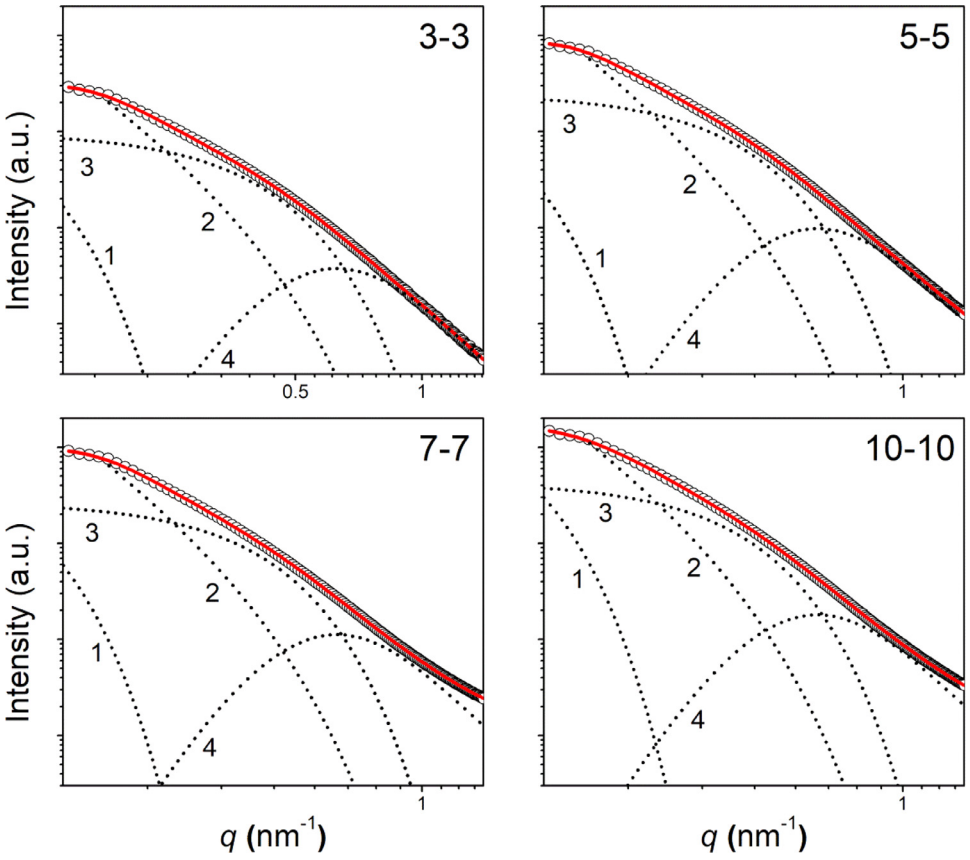

Fig. 6. Dispersion intensity *I(q)* as a function of the moment transfer vector *q* for the composite bilayers. Experimental data (empty symbols); fitting of Eq. (2) with SASfit package (solid line); different contributions of Beaucage model for selected samples: 1) Guinier aggregates, 2) Porod aggregates, 3) Guinier individual particles, 4) Porod individual particles.

the films (two bio-polymer layers added to magnetic nanoparicles arranged in clusters of different sizes) makes difficult the analysis of this region by using this relatively simple law. On the other hand, when this analysis was applied to neat MNP (i.e. not embedded into polymeric matrices), their respective radius of gyration and diameter of the agglomerates were calculated as 6 nm and 15.4 nm, respectively, indicating that small aggregation of primary particles also occurs when MNPs are in a colloidal suspension (Kloster et al., 2018). In addition, the scattering intensity in the Porod region presented a slope close to -4, which corresponds to individual particles with smooth surfaces (Kloster et al., 2018).

Therefore, to perform a deeper analysis identifying MNP agglomerates within the matrices, the unified exponential/power-law for two hierarchical structures postulated by Beaucage was used to assess the characteristics of aggregates (until 30 nm due to the q-range used) and primary particles. In this postulate, Guinier and Porod regimes are combined into a single equation to describe the scattering of any morphology of any systems composed by entities of complex morphology containing multiple levels of related structural features (Moscoso Londoño et al., 2017). In our case the following equation was used:

$$I(q) \cong G\ exp\frac{\left(-q^2Rg^2\right)}{3} + B\ exp\frac{\left(-q^2Rs^2\right)}{3}\left(\frac{\left(erf\left(q\ Rg/\sqrt{6}\right)\right)^3}{q}\right)^{Df} + Gs\ exp\frac{\left(-q^2Rs^2\right)}{3} + Bs\left(\frac{\left(erf\left(q\ Rs/\sqrt{6}\right)\right)^3}{q}\right)^{P} \quad (2)$$

where the first term of Eq. 2 describes the large-scale structure of size *Rg*, composed of small subunits of size *Rs*. The second one refers to the mass-fractal regime with two structural limits and the last two terms can be associated with structural information of smaller substructures (primary MNPs). *G* and *B* are the Guinier and Porod pre-factors of those large structures (aggregates). *Gs* and *Bs* are the Guinier and Porod pre-factors of the smaller structures (individual particles). *Rg* is the radius of gyration of large-scale structures with fractal dimension *Df* (surface fractals $4 > Df > 3$), and whose architecture is defined by small particles of size *Rs*. *P* is the exponent of the power law assigned to the smaller structures and *erf* is the error function. For fitting purposes, *P* was set as 4, while *Rs* (single nanoparticle radius) was fixed at 4.8 nm, this last according to TEM information about the size of the synthesized MNP, even though a small variation was allowed during calculation (Kloster et al., 2018, 2020). The good fitting of the experimental SAXS curves of all the bilayers with the Beaucage model (continuous lines) is shown in Fig. 6. The individual contributions of the Guinier and Porod component curves of aggregates (curves 1 and 2) and primary particles (curves 3 and 4) are also included in the plots (dashed lines). Table 1 summarizes the fitting parameters calculated using Software package SASfit for the different bilayers as well as the agglomerate size ξ that was calculated assuming spherical shape.

The pre-factors *B, Gs* and *Bs* increase as the MNP content increase, as the number of small agglomerates is directly related to the amount of iron oxide included in the bilayers. The radius of gyration (related to small aggregate sizes) was found between 19.4 and 21.2 nm and does not seem to be related with the MNP content in the films. Moreover, the *Df* values resulted between 3.04 and 3.17 for all the bilayers. The fractal dimension close to 3 indicates that the agglomerates of individual particles in all composite samples have similar structures that correspond to smooth and compact aggregates (Chen & Teixeira, 1986) with three-dimensional architecture.

3.2. Magnetic characterization

Fig. 7a shows the temperature dependence of the magnetization for three different bilayers recorded at DC field of 50 Oe under the zero-

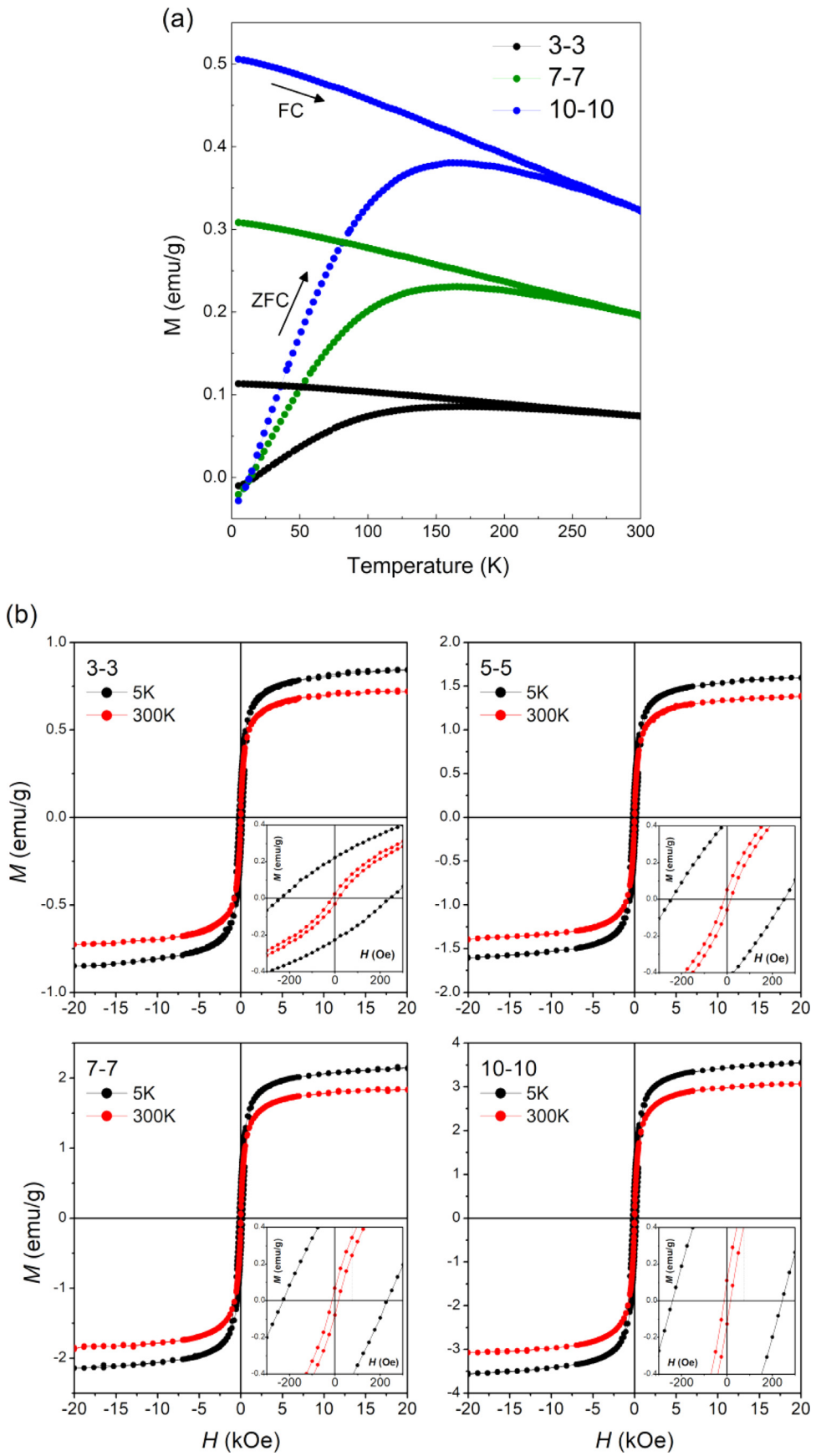

Fig. 7. a) Magnetization as a function of the temperature obtained under the ZFC and FC protocols for selected samples. b) Magnetization curves as a function of the magnetic field at 5 and 300 K.

Table 2
Maximum in the ZFC curves ($T_B^{MAX\ ZFC}$), $<T_B>$ and Ti obtained from the ZFC-FC tests and magnetic anisotropy constant (K).

Bilayer	$T_B^{MAX\ ZFC}$ (K)	$<T_B>$ (K)	T_i (K)	K (kJ/m^3)
3-3	168	73.2	192	46 ± 2
7-7	165	71.1	235	45 ± 2
10-10	162	72.2	253	45 ± 2

field-cooling (ZFC) and field-cooling (FC) protocols. In qualitative terms, the shape of the curves is characteristic of polydispersed systems with high or moderate dipole interactions (Moscoso Londoño et al., 2017). All the ZFC curves exhibit a broad maximum, ($T_B^{MAX\ ZFC}$) located between 162 K and 168 K (see Table 2). Assuming this maximum as the blocking temperature it is possible to affirm that all films are in a superparamagnetic regime above $T_B^{MAX\ ZFC}$ (Moscoso Londoño et al., 2013). The values of the mean blocking temperature $<T_B>$, calculated from the FC/ZFC curves using the derivative expression d(FC-ZFC)/dT and the irreversibility temperatures, T_i (defined as the threshold temperature above which FC and ZFC curves coincide) are also included in Table 2. $<T_B>$ values do not exhibit a clear trend with the MNP content but rather all the films present similar values, indicating that the sizes of magnetic particles or agglomerates are comparable in the bilayers, as was also inferred from SAXS analysis. Some works indicate that both $T_B^{MAX\ ZFC}$ and $<T_B>$ increase with the strengthening of dipole interactions (Sung Lee, Tan, Hua Wu, & Keun Kim, 2011), then, the similarity in the obtained values could be indicating that the magnitude of the dipole interactions remains almost constant as the concentration of nanoparticles changes. By contrast, the irreversibility temperatures (Ti) change by tens of Kelvin with the content of MNP. This fact is commonly associated with a larger polydispersity in the investigated samples, i.e. the formation of larger agglomerates as the MNP concentration increases would increase the Ti, while the remaining amount of individual and well dispersed MNP still present in the bilayers would keep the blocking temperatures in similar values for all samples (Moscoso Londoño et al., 2017). Thus, this behavior could be an evidence of the disordered formation of aggregates of different sizes, as consequence of the increase in the content of nanoparticles. On the other hand, it is interesting to point out that the $<T_B>$ and Ti temperatures obtained for these bilayer films are lower than those registered for the individual composite films (not show here). For chitosan composites with 3, 7 and 10 wt% MNP values of $<T_B>$ were found between 114.0 and 129.1 K and Ti in the range of 260-294 K (Kloster et al., 2018), while magnetic alginate films exhibited $<T_B>$ values between 114.1 and 118.3 K with Ti ranging from 267 to 288 K (Kloster et al., 2020). Such differences confirm that the alginate-chitosan complexation, still taking place at the interface, is an encouraging way to enhance the superparamagnetic behavior of these composites.

According to Néel theory, the blocking temperature is related to the particle volume and the magnetic anisotropy constant (K). This constant includes the contribution from magnetocrystalline (bulk), shape, strain, and surface anisotropies (Nawara et al., 2012). The distribution of blocking temperatures due to differences in MNPs size can be obtained from the ZFC-FC measurements. Since the registered signal is the magnetic moment and thus it is proportional to the magnetic particle volume in the whole sample, if this distribution is weighed by volume and we can obtain the mean value $<T_B>$ weighed by volume. On the other hand, the mean volume weighed by volume (<V>) can be calculated from TEM histogram (obtained for the synthesized MNP and reported in a previous paper (Kloster et al., 2018)). As we have a distribution of nanoparticle sizes, the Néel expression to calculate K leads to:

$$K = log\left(\frac{\tau_m}{\tau_0}\right)\frac{k_B\langle T_B\rangle}{\langle V\rangle} \quad (3)$$

where τ_m is the experimental measuring time (100 s in the present work), τ_0 is the microscopy characteristic time (10^{-9} s) and k_B is the Boltzmann constant.

Equation (3) is valid if the non-dimensional parameter $h = \frac{\mu_0 M_S \rho H}{2K} << 1$, where μ_0 is the vacuum magnetic permeability, M_S the saturation magnetization of the MNP, ρ their density and H the external magnetic field (50 Oe).

Although the systems are not ideal as Néel law requires (Néel theory is valid strictly for non-interacting systems), using the mean blocking temperatures ($<T_B>$) and the mean volume (<V>), the magnetic anisotropy constants (K) for the different bilayers can be calculated. For this purpose, the MNP diameter histogram was fitted with a lognormal distribution (mean: 9.55 nm; standard deviation: 0.12 nm). Then, from this distribution, the weighted average volume per volume was calculated as 556 nm^3 with a standard deviation of 16 nm^3. Thus, the anisotropy constants (K) were calculated for the composite bilayers and are summarized in Table 2, finding in all cases values about 45 kJ/m^3. For all the samples $h \ll 1$. Although the values obtained are in the same order of magnitude to those reported in literature for similar systems (Goya, Berquó, Fonseca, & Morales, 2003; Meiorin et al., 2016; Moscoso Londoño et al., 2013, 2017), it should be pointed out that in this calculation interparticle interactions (that seems to be important in our systems) were not taken into account and thus it could result in values not as exact as we would like to obtain (Moscoso Londoño et al., 2017).

Curves of magnetization as a function of the applied magnetic field (M vs H), obtained at two different temperatures (5 and 300 K) for selected bilayer films are shown in Fig. 7b. In all cases, the typical features of systems composed by monodomain nanoparticles can be noticed: a coercive field (Hc) at low temperature (5 K), and the expected S-shape without hysteresis at 300 K (Allia et al., 2001; Knobel et al., 2008). At low temperature the system is thermally blocked and thus, magnetic relaxation time is longer than measurement time. At room temperature, the magnetic relaxation time is shorter than the measurement time and the particle ensembles behave as a paramagnetic system (Moscoso Londoño et al., 2013). The saturation magnetization (Ms) values per gram of sample at both temperatures, as well as the coercive fields at 5 K are reported in Table 3. The saturation magnetization values are larger at 5 K and increase as the MNP content increases, as expected.

Using the Ms of the composite bilayers and the Ms of the neat MNP (57.7 emu/g at 5 K and 49.9 emu/g at 300 K, (Kloster et al., 2020)) we calculated the actual content of magnetic material (AMM) in the bilayers and included the values in Table 3. The AMM obtained using the saturation magnetization values at both temperatures are very similar since the nanoparticles' magnetization should be the same for all the samples because the MNP used came from the same batch. However, the calculated AMM are much lower than the nominal MNP content, which implies that not all the MNP added to the corresponding film forming

Table 3
Saturation magnetization (Ms) at 5 and 300 K, actual MNP content calculated from Ms values (AMM) and coercivity (Hc).

	M (H=±20 kOe) at 5K *(emu/g)*	% AMM calculated from Ms (5K)	M (H=±20 kOe) at 300K *(emu/g)*	% AMM calculated from Ms (300K)	% AMM (average value)	Hc at 5K *(Oe)*
3-3	0.84	1.46	0.72	1.45	1.45 ± 0.01	243
5-5	1.59	2.76	1.37	2.75	2.76 ± 0.01	255
7-7	2.14	3.71	1.83	3.66	3.69 ± 0.04	231
10-10	3.55	6.15	3.08	6.16	6.16 ± 0.01	245

suspensions were efficiently transferred to the bilayer films, as was also noticed in previous works (Kloster et al., 2018, 2020). In this regards, the "in situ" method for obtaining nanocomposite films has clear advantages with respect to the procedure selected in the present case, but the impossibility of precipitating the magnetic iron oxide by immersing the film in the NaOH aqueous solution (Kloster, Marcovich, et al., 2015) after forming the alginate layer restricts its application in the present case (Kloster et al., 2017). On the other hand, the synthesis of magnetic particles and posterior incorporation into the film forming polymeric solutions lead to weaker interaction between matrix and particles/clusters than the “in situ” synthesis (Kloster et al., 2018) and in this way, the magnetic entities are freer to react in the presence of an external magnetic field. In addition, this last method allows a better control of the amount of plasticizer required in the films that can significantly affect some specific properties. On the other hand, it can be considered the addition of emulsifying agents to the individual film forming suspensions that lead to the obtaining of stable colloidal suspensions; however, it would add an additional variable that could further modify the behavior of this complex system.

4. Conclusions

Magnetic bilayer films using chitosan and alginate as bio-based polymeric matrices of each layer were obtained by casting of film forming suspensions containing different amounts of iron oxide nanoparticles. Different characterization techniques indicated that the magnetic phase is quite well dispersed in the carbohydrate matrices but arranged in scattering structures of different sizes. Although the polymers interact only in the interface, within a small thickness compared with that of the total bilayer, the combination of carbohydrates of different ionic nature leads to the formation of an outstanding polyionic complex. The bilayer material appears to be beneficial regarding the magnetic behavior of the composite samples, since they presented reduced mean blocking and irreversibility temperatures in comparison with those found when just one of the polymers was used as matrix.

Declaration of competing interest

The authors declare that they have no known competing financial interests or personal relationships that could have appeared to influence the work reported in this paper.

Acknowledgements

The authors gratefully acknowledge the financial support provided by the Consejo Nacional de Investigaciones Científicas y Técnicas (CONICET, Grant PIP # 0677), the Agencia Nacional de Promoción Científica y Tecnológica (ANPCyT, Grant PICT-2016-2034 and 2017-1318) and the Universidad Nacional de Mar del Plata (Project # 15/G557 - ING561/19). The work at UNICAMP was supported by FAPESP (2014/26672-8; 17/10581-1) and CNPq Brazil. Small-angle X-ray scattering data were acquired at beamline SAXS1 (proposal 20160488) at Brazilian Synchrotron Light Laboratory (LNLS).

Data availability

The data that support the findings of this study are available from the corresponding author upon reasonable request.

References

Abbaszad Rafi, A., & Mahkam, M (2015). Preparation of magnetic pH-sensitive film with alginate base for colon specific drug delivery. *International Journal of Polymeric Materials and Polymeric Biomaterials, 64*(4), 214–219. https://doi.org/10.1080/00914037.2014.936593.

Agostini de Moraes, M., Cocenza, D. S., da Cruz Vasconcellos, F., Fraceto, L. F., & Beppu, M. M. (2013). Chitosan and alginate biopolymer membranes for remediation of contaminated water with herbicides. *Journal of Environmental Management, 131*, 222–227. https://doi.org/10.1016/j.jenvman.2013.09.028.

Allia, P., Coisson, M., Tiberto, P., Vinai, F., Knobel, M., Novak, M., & Nunes, W. (2001). Granular Cu-Co alloys as interacting superparamagnets. *Physical Review B, 64*(14), 1–12. https://doi.org/10.1103/PhysRevB.64.144420.

Bartůněk, V., Sedmidubský, D., Huber, Š., Švecová, M., Ulbrich, P., & Jankovský, O. (2018). Synthesis and properties of nanosized stoichiometric cobalt ferrite spinel. *Materials, 11*(7), 1241. https://doi.org/10.3390/ma11071241.

Bhatt, A. S., Krishna Bhat, D., & Santosh, M. S (2010). Electrical and magnetic properties of chitosan-magnetite nanocomposites. *Physica B: Condensed Matter, 405*(8), 2078–2082. https://doi.org/10.1016/j.physb.2010.01.106.

Brazel, C. S. (2009). Magnetothermally-responsive Nanomaterials: Combining magnetic nanostructures and thermally-sensitive polymers for triggered drug release. *Pharmaceutical Research, 26*(3), 644–656. https://doi.org/10.1007/s11095-008-9773-2.

Carneiro, R. T. A., Taketa, T. B., Gomes Neto, R. J., Oliveira, J. L., Campos, E. V. R., de Moraes, M. A., …, & Fraceto, L. F. (2015). Removal of glyphosate herbicide from water using biopolymer membranes. *Journal of Environmental Management, 151*, 353–360.

Cesano, F., Fenoglio, G., Carlos, L., & Nisticò, R. (2015). One-step synthesis of magnetic chitosan polymer composite films. *Applied Surface Science, 345*, 175–181. https://doi.org/10.1016/j.apsusc.2015.03.154.

Chang, J. J., Lee, Y. H., Wu, M. H., Yang, M. C., & Chien, C. T. (2012). Electrospun antiadhesion barrier made of chitosan alginate for reducing peritoneal adhesions. *Carbohydrate Polymers, 88*(4), 1304–1312. https://doi.org/10.1016/j.carbpol.2012.02.011.

Chen, J., Yang, P., Ma, Y., & Wu, T. (2011). Characterization of chitosan magnetic nanoparticles for in situ delivery of tissue plasminogen activator. *Carbohydrate Polymers, 84*(1), 364–372. https://doi.org/10.1016/j.carbpol.2010.11.052.

Chen, S.-H., & Teixeira, J. (1986). Structure and fractal dimension of protein-detergent complexes. *Physical Review Letters, 57*(20), 2583–2586. https://doi.org/10.1103/PhysRevLett.57.2583.

Cocenza, D. S., De Moraes, M. A., Beppu, M. M., & Fraceto, L. F. (2012). Use of biopolymeric membranes for adsorption of paraquat herbicide from water. *Water, Air, and Soil Pollution, 223*(6), 3093–3104. https://doi.org/10.1007/s11270-012-1092-x.

Cornell, R. M., & Schwertmann, U. (2003). *The Iron Oxides: Structure, Properties, Reactions, Occurrences and Uses* (2nd ed.). John Wiley & Sons.

Criado, M., Rebollar, E., Nogales, A., Ezquerra, T. A., Boulmedais, F., & Mijangos, C. (2016). Quantitative nanomechanical properties of multilayer films made of polysaccharides through spray assisted layer-by-layer assembly. *Biomacromolecules, 18*(1), 169–177. https://doi.org/10.1021/acs.biomac.6b01449.

Daemi, H., Barikani, M., & Barmar, M. (2013). Compatible compositions based on aqueous polyurethane dispersions and sodium alginate. *Carbohydrate Polymers, 92*(1), 490–496. https://doi.org/10.1016/j.carbpol.2012.09.046.

Dong, Y., Liu, H. Z., Xua, L., Li, G., Ma, Z. N., Han, F., …, & Li, S. M. (2010). A novel CHS/ALG bi-layer composite membrane with sustained antimicrobial efficacy used as wound dressing. *Chinese Chemical Letters, 21*(8), 1011–1014. https://doi.org/10.1016/j.cclet.2010.04.010.

Edelman, E. R., & Langer, R. (1993). Optimization of release from magnetically controlled polymeric drug release devices. *Biomaterials, 14*(8), 621–626.

Eivazzadeh-Keihan, R., Radinekiyan, F., Asgharnasl, S., Maleki, A., & Bahreinizad, H. (2020). A natural and eco-friendly magnetic nanobiocomposite based on activated chitosan for heavy metals adsorption and the in-vitro hyperthermia of cancer therapy. *Journal of Materials Research and Technology, 9*(6), 12244–12259. https://doi.org/10.1016/j.jmrt.2020.08.096.

Elmotasem, H. (2008). Chitosan – alginate blend films for the transdermal delivery of meloxicam. *Asian Journal of Pharmaceutical Sciences, 3*, 12–29 (September 2007).

Fang, C., Bhattarai, N., Sun, C., & Zhang, M. (2009). Functionalized Nanoparticles with Long-Term Stability in Biological Media. *Small, 5*(14), 1637–1641. https://doi.org/10.1002/smll.200801647.

George, A., Sanjay, M. R., Sriusk, R., Parameswaranpillai, J., & Siengchin, S. (2020). A comprehensive review on chemical properties and applications of biopolymers and their composites. *International Journal of Biological Macromolecules, 154*, 329–338. https://doi.org/10.1016/j.ijbiomac.2020.03.120.

Gonzalez, J. S., Mijangos, C., & Hernandez, R. (2019). Polysaccharide Coating of Gelatin Gels for Controlled BSA Release. *Polymers, 11*(4), 702.

Goya, G. F., Berquó, T. S., Fonseca, F. C., & Morales, M. P. (2003). Static and dynamic magnetic properties of spherical magnetite nanoparticles. *Journal of Applied Physics, 94*(5), 3520–3528. https://doi.org/10.1063/1.1599959.

Guo, C., Hu, Y., Qian, H., Ning, J., & Xu, S. (2011). Magnetite (Fe_3O_4) tetrakaidecahedral microcrystals: Synthesis , characterization, and micro-Raman study. *Materials Characterization, 62*(1), 148–151. https://doi.org/10.1016/j.matchar.2010.10.016.

Han, F., Dong, Y., Song, A., Yin, R., & Li, S. (2014). Alginate/chitosan based bilayer composite membrane as potential sustained-release wound dressing containing ciprofloxacin hydrochloride. *Applied Surface Science, 311*, 626–634. https://doi.org/10.1016/j.apsusc.2014.05.125.

Iram, M., Guo, C., Guan, Y., Ishfaq, A., & Liu, H. (2010). Adsorption and magnetic removal of neutral red dye from aqueous solution using Fe3O4 hollow nanospheres. *Journal of Hazardous Materials, 181*(1–3), 1039–1050. https://doi.org/10.1016/j.jhazmat.2010.05.119.

Kanti, P., Srigowri, K., Madhuri, J., Smitha, B., & Sridhar, S. (2004). Dehydration of ethanol through blend membranes of chitosan and sodium alginate by pervaporation. *Separation and Purification Technology, 40*(3), 259–266. https://doi.org/10.1016/j.seppur.2004.03.003.

Karimi, Z., Karimi, L., & Shokrollahi, H. (2013). Nano-magnetic particles used in biomedicine : Core and coating materials. *Materials Science & Engineering C, 33*(5), 2465–2475. https://doi.org/10.1016/j.msec.2013.01.045.

Kaya, M., Baran, T., Mentes, A., Asaroglu, M., Sezen, G., & Tozac, K. O. (2014). Extraction and characterization of α-chitin and chitosan from six different aquatic invertebrates. *Food Biophysics, 9*, 145–157. https://doi.org/10.1007/s11483-013-9327-y.

Kloster, G. A., Marcovich, N. E., & Mosiewicki, M. A. (2015). Composite films based on chitosan and nanomagnetite. *European Polymer Journal, 66*, 386–396. https://doi.org/10.1016/j.eurpolymj.2015.02.042.

Kloster, G. A., Muraca, D., Londoño, O. M., Knobel, M., Marcovich, N. E., & Mosiewicki, M. A. (2018). Structural analysis of magnetic nanocomposites based on chitosan. *Polymer Testing, 72*, 202–213. https://doi.org/10.1016/j.polymertesting.2018.10.022.

Kloster, G. A., Muraca, D., Londoño, O. M., Pirota, K. R., Mosiewicki, M. A., & Marcovich, N. E. (2020). Alginate based nanocomposites with magnetic properties. *Composites Part A, 135*(January), Article 105936. https://doi.org/10.1016/j.compositesa.2020.105936.

Kloster, G. A., Muraca, D., Meiorin, C., Pirota, K. R., Marcovich, N. E., & Mosiewicki, M. A. (2015). Magnetic characterization of chitosan – magnetite nanocomposite films. *European Polymer Journal, 72*, 202–211. https://doi.org/10.1016/j.eurpolymj.2015.09.014.

Kloster, G. A., Muraca, D., Mosiewicki, M. A., & Marcovich, N. E. (2017). Magnetic composite films based on alginate and nano-iron oxide particles obtained by synthesis “in situ. *European Polymer Journal, 94*, 43–55.

Knobel, M., Nunes, W. C., Socolovsky, L. M., Biasi, E. De, Vargas, J. M., & Denardin, J. C (2008). Superparamagnetism and other magnetic features in granular materials: A review on ideal and real systems. *Journal of Nanoscience and Nanotechnology, 8*, 2836–2857. https://doi.org/10.1166/jnn.2008.

Lacerda, L., Parize, A. L., Fávere, V., Laranjeira, M. C. M., & Stulzer, H. K (2014). Development and evaluation of pH-sensitive sodium alginate/chitosan microparticles containing the antituberculosis drug rifampicin. *Materials Science and Engineering C, 39*(1), 161–167. https://doi.org/10.1016/j.msec.2014.01.054.

Lakouraj, M. M., Mojerlou, F., & Zare, E. N. (2014). Nanogel and superparamagnetic nanocomposite based on sodium alginate for sorption of heavy metal ions. *Carbohydrate Polymers, 106*(1), 34–41. https://doi.org/10.1016/j.carbpol.2014.01.092.

Lassalle, V. L., Zysler, R. D., & Ferreira, M. L. (2011). Novel and facile synthesis of magnetic composites by a modified co-precipitation method. *Materials Chemistry and Physics, 130*(1–2), 624–634. https://doi.org/10.1016/j.matchemphys.2011.07.035.

Li, J., Jiang, B., Liu, Y., Qiu, C., Hu, J., Qian, G., …, & Ngo, H. H. (2017). Preparation and adsorption properties of magnetic chitosan composite adsorbent for Cu^{2+} removal. *Journal of Cleaner Production*. https://doi.org/10.1016/j.jclepro.2017.04.156.

Matet, M., Heuzey, M. C., Pollet, E., Ajji, A., & Avérous, L. (2013). Innovative thermoplastic chitosan obtained by thermo-mechanical mixing with polyol plasticizers. *Carbohydrate Polymers, 95*(1), 241–251. https://doi.org/10.1016/j.carbpol.2013.02.052.

Meiorin, C., Londoño, O. M., Muraca, D., Socolovsky, L. M., Pirota, K. R., Aranguren, M. I., …, & Mosiewicki, M. A. (2016). Magnetism and structure of nanocomposites made from magnetite and vegetable oil based polymeric matrices. *Materials Chemistry and Physics, 175*, 81–91. https://doi.org/10.1016/j.matchemphys.2016.02.071.

Meiorin, C., Muraca, D., Pirota, K. R., Aranguren, M. I., & Mosiewicki, M. A. (2014). Nanocomposites with superparamagnetic behavior based on a vegetable oil and magnetite nanoparticles. *European Polymer Journal, 53*, 90–99. https://doi.org/10.1016/j.eurpolymj.2014.01.018.

Moscoso Londoño, O., Gonzalez, J. S., Muraca, D., Hoppe, C. E., Alvarez, V. A., López-Quintela, A., …, & Pirota, K. R. (2013). Structural and magnetic behavior of ferrogels obtained by freezing thawing of polyvinyl alcohol/poly(acrylic acid) (PAA)-coated iron oxide nanoparticles. *European Polymer Journal, 49*(2), 279–289. https://doi.org/10.1016/j.eurpolymj.2012.11.007.

Moscoso Londoño, O., Tancredi, P., Muraca, D., Mendoza Zélis, P., Coral, D., Fernández van Raap, M. B., …, & Socolovsky, L. M. (2017). Different approaches to analyze the dipolar interaction effects on diluted and concentrated granular superparamagnetic systems. *Journal of Magnetism and Magnetic Materials, 428*(August 2016), 105–118. https://doi.org/10.1016/j.jmmm.2016.12.019.

Moscoso Londoño, O., Tancredi, P., Rivas, P., Muraca, D., Socolovsky, L. M., & Knobel, M. (2018). Small-Angle X-Ray scattering to analyze the morphological properties of nanoparticulated systems. In *Handbook of Materials Characterization* (pp. 37–75). Springer. https://doi.org/10.1007/978-3-319-92955-2_2.

Motwani, S. K., Chopra, S., Talegaonkar, S., Kohli, K., Ahmad, F. J., & Khar, R. K. (2008). Chitosan-sodium alginate nanoparticles as submicroscopic reservoirs for ocular delivery: Formulation, optimisation and in vitro characterisation. *European Journal of Pharmaceutics and Biopharmaceutics, 68*(3), 513–525. https://doi.org/10.1016/j.ejpb.2007.09.009.

Nassar, N. N. (2010). Rapid removal and recovery of Pb (II) from wastewater by magnetic nanoadsorbents. *Journal of Hazardous Materials, 184*(1–3), 538–546. https://doi.org/10.1016/j.jhazmat.2010.08.069.

Nawara, K., Romiszewski, J., Kijewska, K., Szczytko, J., Twardowski, A., Mazur, M., & Krysinski, P. (2012). Adsorption of doxorubicin onto citrate-stabilized magnetic nanoparticles. *The Journal of Physical Chemistry C, 116*, 5598–5609.

Norajit, K., Kim, K. M., & Ryu, G. H. (2010). Comparative studies on the characterization and antioxidant properties of biodegradable alginate films containing ginseng extract. *Journal of Food Engineering, 98*(3), 377–384. https://doi.org/10.1016/j.jfoodeng.2010.01.015.

Patterson, A. L. (1939). The Scherrer formula for X-ray particle size determination. *Physical Review, 56*(10), 978.

Pawlak, A., & Mucha, M. (2003). Thermogravimetric and FTIR studies of chitosan blends. *Thermochimica Acta, 396*(1–2), 153–166. https://doi.org/10.1016/S0040-6031(02)00523-3.

Pereda, M., Aranguren, M. I., & Marcovich, N. E. (2007). Characterization of chitosan/caseinate films. *J. Appl. Polym. Sci., 107*, 1080–1090. https://doi.org/10.1002/app.27052.

Piosik, E., Klimczak, P., Ziegler-borowska, M., & Chełminiak-dudkiewicz, D. (2020). A detailed investigation on interactions between magnetite nanoparticles functionalized with aminated chitosan and a cell model membrane. *Materials Science & Engineering C, 109*, Article 110616. https://doi.org/10.1016/j.msec.2019.110616.

Rafiee, A., Alimohammadian, M. H., Gazori, T., Riazi-rad, F., Fatemi, S. M. R., Parizadeh, A., …, & Havaskary, M. (2014). Comparison of chitosan, alginate and chitosan/alginate nanoparticles with respect to their size, stability, toxicity and transfection. *Asian Pacific Journal of Tropical Disease, 4*(5), 372–377. https://doi.org/10.1016/S2222-1808(14)60590-9.

Reinas, A. E., Hoscheid, J., Outuki, P. M., Lane, M., & Cardoso, C. (2014). Preparation and characterization of microcapsules of Pterodon pubescens Benth . by using natural polymers. *Brazilian Journal of Pharmaceutical Sciences, 50*, 919–930.

Sanna, V., Roggio, A. M., Siliani, S., Piccinini, M., Marceddu, S., Mariani, A., & Sechi, M. (2012). Development of novel cationic chitosan- and anionic alginate — coated poly(D,L-lactide-co- glycolide) nanoparticles for controlled release and light protection of resveratrol. *International Journal of Nanomedicine, 7*, 5501–5516.

Shebanova, O. N., & Lazor, P. (2003). Raman study of magnetite (Fe3O4): laser-induced thermal effects and oxidation. *Journal of Raman Spectroscopy, 34*, 845–852. https://doi.org/10.1002/jrs.1056.

Siddiqui, S. I., & Chaudhry, S. A. (2017). Iron oxide and its modified forms as an adsorbent for arsenic removal: A comprehensive recent advancement. *Process Safety and Environmental Protection, 111*, 592–626. https://doi.org/10.1016/j.psep.2017.08.009.

Slavov, L., Abrashev, M. V, Merodiiska, T., Gelev, C., Vandenberghe, R. E., & Markova-deneva, I. (2010). Raman spectroscopy investigation of magnetite nanoparticles in ferrofluids. *Journal of Magnetism and Magnetic Materials, 322*(14), 1904–1911. https://doi.org/10.1016/j.jmmm.2010.01.005.

Smitha, B., Sridhar, S., & Khan, A. A. (2005). Chitosan-sodium alginate polyion complexes as fuel cell membranes. *European Polymer Journal, 41*(8), 1859–1866. https://doi.org/10.1016/j.eurpolymj.2005.02.018.

Sung Lee, J., Tan, R. P., Hua Wu, J., & Keun Kim, Y. (2011). Effect of interparticle interactions and size dispersion in magnetic nanoparticle assemblies : A static and dynamic study Effect of interparticle interactions and size dispersion in magnetic nanoparticle assemblies : A static and dynamic study. *Applied Physics Letters, 99*, Article 062506. https://doi.org/10.1063/1.3624833.

Szczerba, W., Costo, R., Veintemillas-Verdaguer, S., Del Puerto Morales, M., & Thünemann, A. F. (2017). SAXS analysis of single-and multi-core iron oxide magnetic nanoparticles. *Journal of Applied Crystallography, 50*, 481–488. https://doi.org/10.1107/S1600576717002370.

Tian, K., Xie, C., & Xia, X. (2013). Chitosan/alginate multilayer film for controlled release of IDM on Cu/LDPE composite intrauterine devices. *Colloids and Surfaces B: Biointerfaces, 109*, 82–89. https://doi.org/10.1016/j.colsurfb.2013.03.036.

Wang, L., Sun, Y., & Yang, X. (2014). Fabrication and characterization of ZnxCd1-xS nanoparticles in chitosan alginate nanocomposite films. *Ceramics International, 40*(3), 4869–4873. https://doi.org/10.1016/j.ceramint.2013.09.036.

Wang, Z., Downs, R. T., Pischedda, V., Shetty, R., Saxena, S. K., Zha, C. S., …, & Waskowska, A. (2003). High-pressure x-ray diffraction and Raman spectroscopic studies of the tetragonal spinel CoFe2O4. *Physical Review B, 68*, Article 094101. https://doi.org/10.1103/PhysRevB.68.094101.

Wiercigroch, E., Szafraniec, E., Czamara, K., Pacia, M. Z., Majzner, K., Kochan, K., …, & Malek, K. (2017). Raman and infrared spectroscopy of carbohydrates: A review. *Spectrochimica Acta Part A: Molecular and Biomolecular Spectroscopy, 185*, 317–335. https://doi.org/10.1016/j.saa.2017.05.045.

Xu, P., Zeng, G. M., Huang, D. L., Feng, C. L., Hu, S., Zhao, M. H., …, & Liu, Z. F. (2012). Use of iron oxide nanomaterials in wastewater treatment: A review. *Science of the Total Environment, 424*, 1–10. https://doi.org/10.1016/j.scitotenv.2012.02.023.

Xu, X. Q., Shen, H., Xu, J. R., Xie, M. Q., & Li, X. J. (2006). The colloidal stability and core-shell structure of magnetite nanoparticles coated with alginate. *Applied Surface Science, 253*(4), 2158–2164. https://doi.org/10.1016/j.apsusc.2006.04.015.

Xuan Nui, P., Tan Phuoc, N., Tuyet Nhung, P., Thi Thuy Nga, T. T., & hi Van Thi, T. (2016). Synthesis and characterization of chitosan- coated magnetite nanoparticles and their application in curcumin drug delivery. *Advances in Natural Sciences: Nanoscience and Nanotechnology, 7*(4), 1–9. https://doi.org/10.1088/2043-6262/7/4/045010.

Zając, A., Hanuza, J., Wandas, M., & Dymińska, L. (2015). Determination of N-acetylation degree in chitosan using Raman spectroscopy. *Spectrochimica Acta - Part A: Molecular and Biomolecular Spectroscopy, 134*, 114–120. https://doi.org/10.1016/j.saa.2014.06.071.

Zhang, L., Zhu, X., Sun, H., Chi, G., Xu, J., & Sun, Y. (2010). Control synthesis of magnetic Fe3O4 – chitosan nanoparticles under UV irradiation in aqueous system. *Current Applied Physics, 10*, 828–833. https://doi.org/10.1016/j.cap.2009.10.002.

Zhu, J., Wu, H., & Sun, Q. (2019). Preparation of crosslinked active bilayer film based on chitosan and alginate for regulating ascorbate-glutathione cycle of postharvest cherry tomato (Lycopersicon esculentum). *International Journal of Biological Macromolecules, 130*, 584–594. https://doi.org/10.1016/j.ijbiomac.2019.03.006.

Zvezdova, D. (2010). Synthesis and characterization of chitosan from marine sources in Black Sea. *Annual Proceedings," Angel Kanchev" University of Ruse, 49*, 65–69 *9.1*.